ECF22 - Loading and Environmental effects on Structural Integrity

Effect of the geometrical defectiveness on the mechanical properties of SLM biomedical Ti6Al4V lattices

M. Dallago[a]*, F. Zanini[b], S. Carmignato[b], D. Pasini[c], M. Benedetti[a]

[a]Department of Industrial Engineering, University of Trento, Trento, Italy
[b]Department of Management and Engineering, University of Padova, Stradella San Nicola 3, Vicenza, Italy
[c]Department of Mechanical Engineering, McGill University, Montreal, Quebec, Canada

Abstract

Metallic lattice biomaterials can be very complex structures that are often impossible to be fabricated with other manufacturing technologies than additive manufacturing (AM). Residual stresses and geometric defects such as severe notches and distorted struts are inevitably introduced into the printed structures and these can affect the mechanical and biological properties. Micro X-ray Computed Tomography (μCT) has been proven to be a very powerful tool for accurately measuring the mismatch between the as-designed CAD model and the SLM structure. In this work, selective laser melting (SLM) Ti6Al4V lattices were measured using a metrological μCT system to identify and classify the geometrical distortions introduced by the printing process. The μCT measurements have also been used to build Finite Element (FE) models based on beam elements that make possible a quantification of the effect of these defects on the elastic modulus of the lattice by comparison with FE models based on the ideal geometry. Moreover, solid FE models of the junctions between the struts have been built by importing the CT data in Ansys® to calculate the stress concentrations caused by the severe notches.

Keywords: Cellular materials; Computed tomography; Finite elements; Selective laser melting

1. Introduction

The use of metallic cellular materials in structural components is increasing in the biomedical, aeronautical, automotive sectors (Zhao et al., 2016a) thanks to the advent of additive manufacturing that makes possible to obtain

---

* Corresponding author. Tel.: +0-000-000-0000 ; fax: +0-000-000-0000 .
  E-mail address: michele.dallago@unitn.it

highly porous cellular structures with finely tunable mechanical properties. Among the various AM techniques, SLM allows greater precision (Tan et al., 2017); nevertheless, geometric imperfections are typically present as non-uniform strut thickness, strut waviness and surface irregularities such as notches (Liu, 2017; Zargarian, 2016; Zhao et al., 2016b). These defects are measurable as an as-built/as-designed morphological mismatch that is reflected as a difference between the mechanical properties predicted based on the as-designed geometry and the experimental results, the latter strongly correlating with the number and severity of defects (Bagheri, 2017; Liu, 2017; Parthasarathy, 2010; Van Bael, 2011). This mismatch is related to the SLM process parameters such as the laser power, the scanning speed (Mullen, 2009; Qiu, 2015; Sing, 2018), the layer thickness (Sing, 2018) and the inclination of the struts to the printing plane (Emmelmann, 2011; Mullen, 2009; Pyka, 2013, Yan, 2014).

In this work, μCT was used to carry out a metrological characterization of an SLM Ti6Al4V regular cubic lattice specimen. Micro X-ray computed tomography is an advanced measuring technique that can effectively perform non-destructive evaluations of AM components characterized by inner geometries and internal porosity, including cellular specimens (Wits, 2016; Khademzadeh, 2016). A statistical analysis was carried out on the high-density point clouds extracted from μCT data and the results were used to classify the geometric imperfections and thus devise FE models that include some or all the defects identified. The comparison of the different FE models gives some insight on the effect of geometric defects on the elastic properties and on the stress concentration at the junctions.

2. Materials and experimental

2.1. Cellular specimen

The cellular structure studied in this work is the regular cubic (Figure 1). The lattice was designed with care in eliminating every sharp notch. The cross-section of the cell walls is thus circular (diameter t_0), and all the junctions are filled with the same nominal radius (R), as shown in Figure 1a. The cell wall length is L. The relative density of the lattice is 6.61%. The specimen is provided with threaded heads for gripping purposes (Figure 1b).
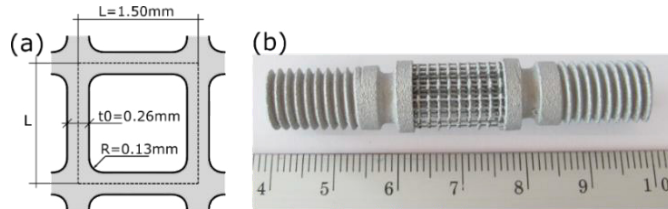

Figure 1. (a) Geometrical parameters of the regular cubic lattice and actual values; (b) Specimen with the threaded heads.

This structure is intended to be employed in the production of fatigue resistant fully porous orthopaedic implants and is designed using the Finite Elements method to obtain an elastic modulus of 3 GPa, to match that of trabecular bone (Dallago, Fontanari, et al., 2018; Dallago, Fontanari, Winiarski, et al., 2017). The specimen was additively manufactured via SLM starting from biomedical grade Ti6Al4V ELI (Grade 23) powder of mean diameter of 8.64 μm. The specimens were built inclined of 45° to the printing direction (Figure 2) using a 3D System ProX DMP 300 printer. Further details are provided in Benedetti (2017). The specimen was treated by hot isostatic pressing (HIP) at 920 °C and 1000 bar for 2 hours.
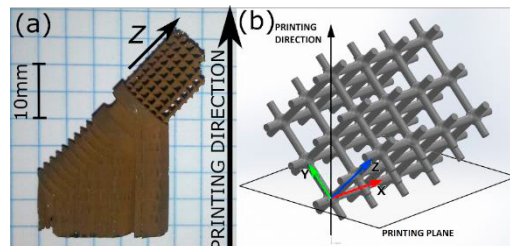

Figure 2. (a) Part of specimen with support structures that show the printing direction; (b) *xyz* reference system associate with the struts: the *x* struts lay in the printing plane while the *y* and *z* struts are inclined of 45°.

2.2. μCT dimensional evaluation

The central cellular part of the specimens was scanned using a metrological μCT system (Nikon Metrology MCT225) characterized by micro-focus X-ray tube, 16-bit detector with 2000×2000 pixels, high-precision linear guideways and controlled cabinet temperature. The voxel size (i.e. the size of the volumetric pixel) of the reconstructed three-dimensional models was equal to 8.3 μm.

3. Results and discussion

3.1. μCT metrological analysis and geometric defects

An in-house Matlab (MathWorks, USA) routine was used to analyze the high-density point clouds extracted from the μCT scanned volumes (an example of portion of the scanned specimen is shown in Figure 3a) and then to carry out a statistical analysis. An *xyz* reference system is defined with the axes parallel to the struts, as shown in Figure 2b and Figure 3a, to correlate the strut direction with the printing direction. The centers of the junctions between the struts were estimated as the centroid of the data points of the 6 struts converging in the junction. Ten sections were sampled along each strut of the specimen and the following geometric parameters were measured (for clarity, only seven shown in Figure 3b):

- Cross-section equivalent radius (calculated as the radius of the circumference with the same area as the strut cross-section).
- Cross-section eccentricity $e = \sqrt{a^2 - b^2}/a$, where a and b are the major and minor axis of the best fitting ellipse, respectively. $e=0$ is a perfect circle while $e=1$ is a segment.
- Cross section orientation with respect to the *xyz* reference system.
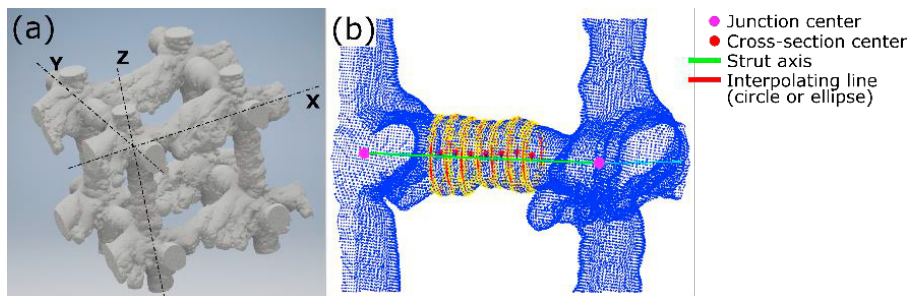- Offset of the cross-section center to the strut axis.

Figure 3. (a) CT of a part of the specimen with *xyz* reference system; (b) CT data cloud with sections, section centers and strut axis highlighted. Note the waviness of the strut (offset between the section centers and the strut axis).

The μCT analysis showed that there is a mismatch between the as-built and the as-designed lattices, due to an excess of material in some parts of the lattice and lack of material in other. This uneven material distribution is ultimately determined by the local heat transfer properties of the powder-solid material system and it shows as a series of defects that affect the lattice. In this work, the following defects were observed and classified (refer to Figure 2b for the relationship between the *xyz* system and the printing direction):

- Variable strut cross-section equivalent radius (Figure 4a). The average cross-section equivalent radius is always higher than the as-designed value. The struts parallel to the printing plane (*x*-struts) show the greatest mean deviation from the design value (67%) and the widest distribution. The wider the distribution, the less predictable is the outcome of the printing process.
- Offset of the cross-section centers from the axis connecting two junction centers (Figure 4b). This offset is manifested as strut waviness (Figure 3b) and again the struts parallel to the printing plane (*x*-struts) show the highest average offset (73%) and the widest distribution.
- Strut cross-section eccentricity (Figure 5). The as-built struts are not perfectly circular, but their cross-section tends to be elliptical. The highest value of eccentricity is shown by the *x*-struts (*e=0.79*, Figure 5a), that also

have the major axis of the best fitting ellipse inclined of 45° to the *y* and *z* directions, exactly aligned with the printing direction. The small inclination of the cross-sections of the other struts indicates that most likely the specimen was not printed perfectly at 45° as indicated in Figure 2b.

- Missing/interrupted struts. In this specimen, of 910 struts, two vertical struts are interrupted due to an excessive thinning of the section.
- Junction center position. Due to the uneven distribution of material in the proximity of the junction, the centroid of the same does not coincide with the as-designed position (there is a 35±18 μm offset, which is indeed quite small compared to a 1500 μm unit cell size).
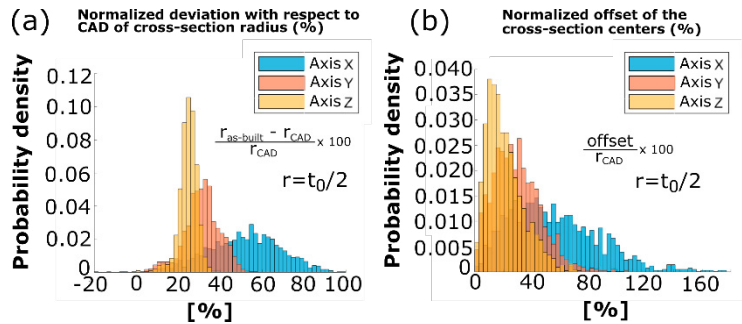

Figure 4. (a) Distribution of the normalized deviation between the as-designed and the as-built cross-section radius; (b) Distribution of the normalized offset between the as-built cross-section center and the strut axis.
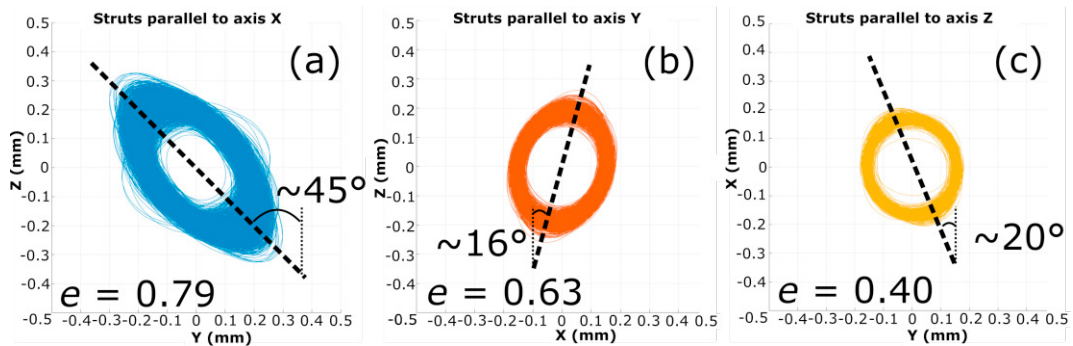

Figure 5. Plot of the best-fitting ellipses of the cross-section of each set of struts. The centers of the sections of each strut are translated to the (0,0) point with the correct inclination to the other two set of struts indicated by the *xyz* reference system. (a) *x*-struts; (b) *y*-struts; (c) *z*-struts.

3.2. Effect of defects on the elastic modulus and the SCF of the lattice: FE analysis

The results of the μCT measurements were used to build FE models (ANSYS®, release 16.1) that include the geometrical defects of the as-built lattice to evaluate their effect on the elastic modulus of the lattice and on the stress concentration at the junctions. Only linear elastic analyses were carried out, using the properties of solid Ti6Al4V ($E = 110$ GPa, $\nu = 0.3$). Models made of solid elements (3D 10-Node Tetrahedral Structural Solid, SOLID187) and beam elements (3 node Timoshenko beam, BEAM189) were both devised (Figure 6). The beam models reproduce the entire specimen and were created by meshing each strut with beam elements with circular cross-section and the section properties (diameter and center offset from the mean axis) assigned based on the statistics extracted from the μCT data (Figure 4d). A normal distribution was assumed, and the values of the strut thickness and offset were assigned randomly based on the mean value and the standard deviation calculated from the μCT data analysis. The simulation consists in a compression test (small displacements). To evaluate the influence of the width of the distribution, the simulations were repeated 15 times for each model type. Four such models were created, of increasing complexity, to compare the effect of the different types of defects (in the first three models, the centers of the junctions are in the as-designed location):

- Beam model with variable cross-section diameter and zero center offset.
- Beam model with variable cross-section center offset and constant diameter, equal to the mean value calculated form the CT data (the mean values are different for struts of different orientation).
- Beam model that combines the two previous defects.
- Beam model that includes all the defects: variable cross-section diameter and offset, missing struts and the junction centers location as calculated form the μCT data.

Solid FE models could only be built of a single unit cell size due to limited computational power and were used to calculate both the elastic modulus and the stress concentration factors. The SCF is defined as the ratio between the peak stress in the junction and the nominal stress (ratio between the area of the unit cell and the reaction force in the vertical direction z):

- CAD FEM (Figure 6a): solid model of the unit cell based on the ideal geometry. Periodic boundaries were applied, as in Dallago, Benedetti, et al. (2017).
- CT FEM: solid model of the unit cell based on the as-built geometry. Eight unit cells were extracted from the CT of the specimen (Figure 6b) and separately tested (Figure 6c). The estimate of the elastic modulus is the average of the eight values. The accuracy of the results is limited by the element size (30÷40 μm), that is chosen to be not far from the CT voxel size, and a convergence analysis was also carried out to verify the stability of the results. The boundary conditions applied to calculate the elastic modulus are shown in Figure 6c. To calculate the SCF, the displacements corresponding to the position of each CT unit cell extracted from the beam model that includes all the defects are applied as boundary conditions.
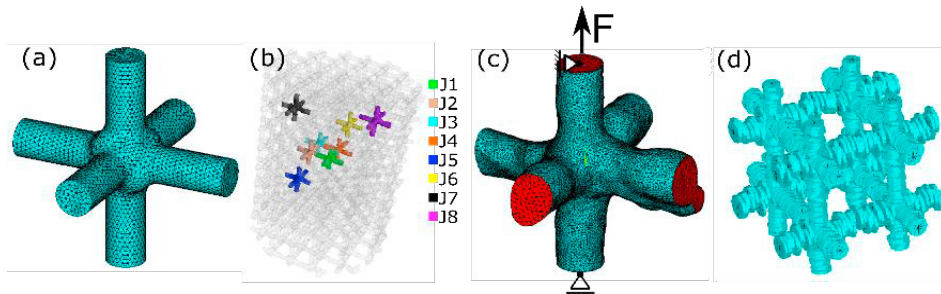

Figure 6. (a) Solid FE unit cell model based on the CAD; (b) CT of the entire specimen with analyzed junctions highlighted; (c) Example of FE mesh of one of the CT unit cells, with boundary conditions to calculate the elastic modulus; (d) part of the beam model that includes the statistical distribution of the defects.

The simulations carried out on the imperfect FE models show the effect of the defects on the elastic modulus (Figure 7). The elastic modulus measured experimentally (Dallago, Fontanari, et al., 2018) is 3436 MPa, which is higher than the elastic modulus calculated from the as-designed model (3020 MPa) due to the thicker struts of the as-built lattice. But the elastic modulus of an ideal unit cell with the struts thickness equal to the as-built mean values is well over 4000MPa, regardless of the fillet radius (Dallago, Fontanari, Torresani, et al., 2017). The lower elastic modulus measured in the experiments is due to the geometric defects. The results of the beam models give some insight on the influence of the geometric defects: interestingly, the offset of the cross-section centers (strut waviness) causes a remarkable drop in the elastic modulus (3766 MPa) compared to the model that accounts only for the cross-section diameter statistical distribution (4264 MPa). In fact, the latter value is not significantly different from the model that includes both the strut waviness and the cross-section diameter statistical distribution (3754 MPa). On the other hand, the elastic modulus of the model that includes all the defects is considerably lower (3411 MPa) and very close to the experimental value and even by adding the two missing vertical struts the elastic modulus increases only to 3562 MPa. In conclusion, the increase in the mean cross section diameter has the obvious effect of increasing the elastic modulus, but it also appears that the width of the cross-section diameter distribution does not have a significant effect (very small standard deviation in the results of the beam models). The strut waviness and the misalignment of the junction centers significantly decrease the elastic modulus while the missing struts, even if parallel to the loading direction, do not have a major effect, if they are few compared to the total number of struts. This is because the strut waviness and the misalignment of the junction centers introduce bending loads in the lattice. It is likely that a stretching

dominated lattice such as the one considered in this work, is particularly sensitive to these types of defects. The results of the solid FEM model based on the CT scans are reasonably close to the experimental value, although slightly higher. This is most likely because only unit-cell sized models could be simulated, that cannot correctly reproduce the complex interaction between the various defect types.
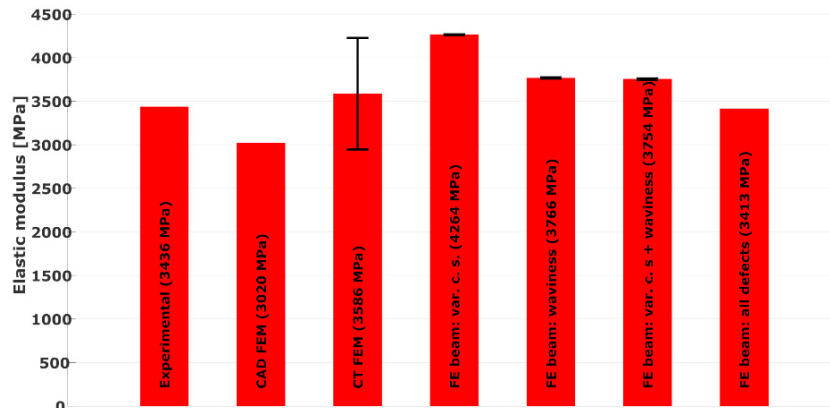

Figure 7. Bar chart comparing the elastic moduli calculated by the various FE models.

The fatigue notch factor measured experimentally for this structure is 188 (Dallago, Fontanari, et al., 2018) that compared to the SCF in the as-designed lattice (62), indicates, in our view, that the notches introduced in these structures due to the manufacturing process are more severe than what can be predicted from the CAD model. The simulations on the as-built junctions show that the stress concentration increased of roughly 21% on average (Table 1), but there is a wide variability. These results prove that the manufacturing process introduces notches in the lattice, but not quite as severe as expected from the fatigue tests. There are several possible reasons for this discrepancy: (i) only a limited number of junctions was analyzed (there may be more severe junctions that are responsible for the failure of the specimens); (ii) detrimental tensile residual stresses (Dallago, Fontanari, et al., 2017); (iii) small distortion of the specimen that may introduce a bending load once the specimen is mounted in the fatigue testing machine; (iv) possible presence of brittle alpha case (Dallago, Fontanari, et al., 2017).

Table 1. SCF calculated from the solid FE models based on the CT unit cells: mean value (μ),
standard deviation (σ) and % deviation on the SCF between the CT and the CAD based FE models.

Junction	μ (SCF CT)	σ (SCF CT)	ΔSCF CT vs CAD
J1	76.02	1.1	21.9%
J2	53.14	1.4	-14.7%
J3	76.75	4.5	23.1%
J4	68.54	0.9	9.9%
J5	76.80	1.0	23.2%
J6	85.00	1.3	36.3%
J7	88.90	1.0	42.7%
J8	80.34	3.8	28.9%
Average	75.67	10.9	21.4%

4. Conclusions

In this work, the authors investigated the effect of the manufacturing defects in cellular lattices on the elastic modulus and the stress concentration at the junctions. The conclusions regarding the defect types and their effect on the elastic modulus are summarized in Table 2.

The uneven distribution of material in the as-built lattice generally has a detrimental effect on the stress concentration at the junctions because sharp notches are created.

Table 2. Summary of the defect types observed in the specimen and their effect on the elastic modulus of the lattice.

Defect type	Description of the defect	Effect on elastic modulus
Strut thickness mismatch	The as-built strut cross-section is irregular, and the mean equivalent diameter does not match the design value.	Depends on whether struts are oversized (increase) or undersized (decrease)
Strut waviness	The barycenter of the cross-section is offset from the strut axis.	decrease
Junction centers offset	The barycenter of the junction between the struts is not located in the junction center of the as-designed lattice.	decrease
Missing struts	Some struts are missing or are interrupted, thus unable to carry any load.	decrease

References

Benedetti, M., Torresani, E., Leoni, M., Fontanari, V., Bandini, M., Pederzolli, C., Potrich, C., 2017. The effect of post-sintering treatments on the fatigue and biological behavior of Ti- 6Al-4V ELI parts made by selective laser melting, J. Mech. Behav. Biomed. Mater. 71, pp. 295–306.

Dallago, M., Benedetti, M., Luchin, V., Fontanari, V., 2017. Orthotropic elastic constants of 2D cellular structures with variously arranged square cells: The effect of filleted wall junctions, International Journal of Mechanical Sciences 122, pp. 63–78.

Dallago, M., Fontanari, V., Torresani, E., Leoni, M., Pederzolli, C., Potrich, C., Benedetti, M., 2018. Fatigue and biological properties of Ti-6Al-4V ELI cellular structures with variously arranged cubic cells made by selective laser melting, Journal of the Mechanical Behavior of Biomedical Materials 78, pp. 381–394.

Dallago, M., Fontanari, V., Winiarski, B., Zanini, F., Carmignato, S., Benedetti, M., 2017. Fatigue properties of Ti6Al4V cellular specimens fabricated via SLM: CAD vs real geometry, Structural Integrity Procedia 7, pp. 116–123.

Emmelmann, C., Scheinemann, P., Munsch, M., Seyda, V., 2011. Laser Additive Manufacturing of Modified Implant Surfaces with Osseointegrative Characteristics, Physics Procedia 12, pp. 375–384.

Khademzadeh, S., Carmignato, S., Parvin, N., Zanini, F., Bariani, P.F. 2016. Micro porosity analysis in additive manufactured NiTi parts using micro computed tomography and electron microscopy. Materials and Design 90, pp. 745-752.

Liu, L., Kamm, P., Garcia-Moreno, F., Banhart, J., Pasini, D., 2017. Elastic and failure response of imperfect three-dimensional metallic lattices: the role of geometric defects induced by Selective Laser Melting, Journal of the Mechanics and Physics of Solids 107, pp. 160–184.

Mullen, L., Stamp, R. C., Brooks, W. K., Jones, E., Sutcliffe, C. J., 2009. Selective Laser Melting: A Regular Unit Cell Approach for the Manufacture of Porous, Titanium, Bone In-Growth Constructs, Suitable for Orthopedic Applications, J Biomed Mater Res B Appl Biomater 89(2), pp. 325–334.

Parthasarathy, J., Starly, B., Ramana, S., Christensen, A., 2010. Mechanical evaluation of porous titanium (Ti6Al4V) structures with electron beam melting (EBM), Journal of the Mechanical Behavior of Biomedical Materials 3, pp. 249–259.

Pyka, G., Kerckhofs, G., Papantoniou, I., Speirs, M., Schrooten, J., Wevers, M., 2013. Surface Roughness and Morphology Customization of Additive Manufactured Open Porous Ti6Al4V Structures, Materials 6, pp. 4737–4757.

Qiu, C., Yue, S., Adkins, N. J. E., Ward, M., Hassanin, H., Lee, P. D., Withers, P. J., Attallah, M. M., 2015. Influence of processing conditionson strut structure and compressive properties of cellular lattice structures fabricated by selective laser melting, Materials Science & Engineering A 628, pp.188–197.

Sing, S. L., Wiria, F. E., Yeong, W. Y., 2018. Selective laser melting of lattice structures: A statistical approach to manufacturability and mechanical behavior, Robotics and Computer–Integrated Manufacturing 49, pp. 170–180.

Tan, X.P., Tan, Y.J., Chow, C.S.L., Tor, S.B., Yeong, W.Y., 2017. Metallic powder-bed based 3D printing of cellular scaffolds for orthopaedic implants: a state-of-the-art review on manufacturing, topological design, mechanical properties and biocompatibility. Mater. Sci. Eng. C 76, 1328–1343.

Van Bael, S., Kerckhofs, G., Moesen, M., Pyka, G., Schrooten, J., Kruth, J.P., 2011. Micro-CT-based improvement of geometrical and mechanical controllability of selective laser melted Ti6Al4V porous structures, Materials Science and Engineering A 528, pp. 7423–7431.

Wits, W. W., Carmignato, S., Zanini, F., Vaneker, T.H.J., 2016. Porosity testing methods for the quality assessment of selective laser melted parts, CIRP Annals Man. Tech. 65(1), pp. 201-204.

Yan, C., Hao, L., Hussein, A., Young, P., Raymont, D., 2014. Advanced lightweight 316L stainless steel cellular lattice structures fabricated via selective laser melting Materials and Design 55, pp. 533–541.

Zargarian, A., Esfahanian, M., Kadkhodapour, J., Ziaei-Rad, S., 2016. Numerical simulation of the fatigue behavior of additive manufactured titanium porous lattice structures, Materials Science and Engineering C 60, pp. 339-347.

Zhao, S., Li, S. J., Hou, W. T., Hao, Y. L., Yang, R., Murr, L. E., 2016a. Microstructure and mechanical properties of open cellular Ti6Al4V prototypes fabricated by electron beam melting for biomedical applications, Materials Technology: Advanced Performance Materials 31 (2), pp. 98–107.

Zhao, X., Li, S., Zhang, M., Liu, Y., Serecombe, T. B., Wang, S., Hao, Y., Yang, R., Murr L. E., 2016b. Comparison of the microstructures and mechanical properties of Ti6Al4V fabricated by selective laser melting and electron beam melting, Materials and Design 95, pp. 21-31.